

Layer-by-Layer Self-Assembled Nanostructured Electrodes for Lithium-Ion Batteries

Zhen Wang,* Armin Vahid Mohammadi, Liangqi Ouyang, Johan Erlandsson, Cheuk-Wai Tai, Lars Wågberg, and Mahiar Max Hamedy*

Gaining control over the nanoscale assembly of different electrode components in energy storage systems can open the door for design and fabrication of new electrode and device architectures that are not currently feasible. This work presents aqueous layer-by-layer (LbL) self-assembly as a route towards design and fabrication of advanced lithium-ion batteries (LIBs) with unprecedented control over the structure of the electrode at the nanoscale, and with possibilities for various new designs of batteries beyond the conventional planar systems. LbL self-assembly is a greener fabrication route utilizing aqueous dispersions that allow various Li^+ intercalating materials assembled in complex 3D porous substrates. The spatial precision of positioning of the electrode components, including ion intercalating phase and electron-conducting phase, is down to nanometer resolution. This capable approach makes a lithium titanate anode delivering a specific capacity of 167 mAh g^{-1} at 0.1C and having comparable performances to conventional slurry-cast electrodes at current densities up to 100C. It also enables high flexibility in the design and fabrication of the electrodes where various advanced multilayered nanostructures can be tailored for optimal electrode performance by choosing cationic polyelectrolytes with different molecular sizes. A full-cell LIB with excellent mechanical resilience is built on porous insulating foams.

Lithium-ion batteries (LIBs) power an increasingly diverse range of applications,^[1] and are currently fabricated by mixing micron-sized particles of lithium-ion intercalators (e.g., lithium cobalt oxide, lithium iron phosphate (LFP), and graphite) and electron conductors (e.g., carbon black) in a random slurry held

together by polymeric binders which is then coated on metallic current collector sheets to form planar electrodes. This electrode processing and fabrication pose two major limitations:

- 1) It limits the form factors of batteries. With the planar structure, the battery has to be either rectangular in shape with the anode, separator and cathode sandwiched, or to be cylindrical in shape, with the sandwich being rolled up. These 2D form factors rule out the potential of battery designs for applications where flexible, stretchable, compressible, and arbitrary shaped batteries are needed.^[2] In addition, the sandwiched 2D batteries must strike a balance between energy density and power density because of the limitation in their 2D footprint area.^[3] This issue could be solved by moving to full 3D battery structures.^[4]
- 2) It does not allow an optimal arrangement of the ion intercalating phase and electron conducting phase in a predetermined structure at the necessary nano-dimensions.^[5] Instead, these phases are randomly mixed as micron-sized particles.

Molecular self-assembly^[6–8] is one, if not the only, route for achieving a scalable fabrication strategy^[9] that overcomes these

Dr. Z. Wang, Dr. L. Ouyang, Dr. J. Erlandsson, Prof. L. Wågberg,
 Dr. M. M. Hamedy
 Division of Fibre Technology
 Department of Fibre and Polymer Technology
 KTH Royal Institute of Technology
 Stockholm 10044, Sweden
 E-mail: zhenwang@kth.se; mahiar@kth.se

 The ORCID identification number(s) for the author(s) of this article can be found under <https://doi.org/10.1002/smll.202006434>.

© 2020 The Authors. Small published by Wiley-VCH GmbH. This is an open access article under the terms of the Creative Commons Attribution-NonCommercial-NoDerivs License, which permits use and distribution in any medium, provided the original work is properly cited, the use is non-commercial and no modifications or adaptations are made.

Dr. A. Vahid Mohammadi
 A. J. Drexel Nanomaterials Institute
 Department of Materials Science and Engineering
 Drexel University
 Philadelphia, PA 19104, USA

Dr. C.-W. Tai
 Department of Materials and Environmental Chemistry
 Stockholm University
 Stockholm 10691, Sweden

Prof. L. Wågberg, Dr. M. M. Hamedy
 Wallenberg Wood Science Centre
 Department of Fibre and Polymer Technology
 KTH Royal Institute of Technology
 Stockholm 10044, Sweden

DOI: 10.1002/smll.202006434

two limitations. A promising and versatile technique for self-assembly is the layer-by-layer (LbL) process which is generally based on the electrostatic or H-bonding interactions between the different compounds.^[9–11] The electrostatic interactions rely mainly on ionically charged and well-dispersed colloids or polyelectrolytes in water. The adsorption in each layer leads to a charge reversal, which allows for the consecutive adsorption of oppositely charged species on top of each other. The driving force behind the adsorption is of entropic origin due to the release of counter ions to the charged species and the alternating adsorption of cationic and anionic components leads to the continuous growth of multilayers. The assembly can be carried out using a wide range of the techniques with capability to deposit each layer within seconds at the meters scale.^[9] One hallmark of LbL assembly is its independence on substrate geometry,^[12] which enables fabrication of electrodes with nanometer precision on complex 3D substrates beyond just planar substrates. A 3D porous structure is especially preferable for electrode substrates of batteries and supercapacitors as their low density does not add much weight to the electrode while their high specific surface area extends the contact area between the active materials and the electrolyte. Currently, LIBs built in the form of porous substrates rely on conductive aerogels.^[13–16] One of the most prevailing methods is in situ fabrication of graphene oxide aerogels that are embedded with electrode materials, such as Fe₃O₄ nanoparticles,^[13] or Fe₂O₃ nanoparticles.^[17] This in situ fabrication of randomly mixed LIB materials into the electrode precludes precise self-assembly as well as the wide range of non-conductive foams and aerogels which are normally ultralow-cost, readily accessible, and mechanically robust.^[18–20] In addition, LbL self-assembly can allow spontaneous positioning of the phases in battery electrodes with nanometer precision due to the interaction among different phases. The process can be performed in water rather than toxic solvents, providing greener and safer electrode processing routes. Therefore, multi-scale assembly can enable fabrication of the entire battery onto a wide range of materials surface,^[18,21] towards true 3D LIBs.

Very little attention, however, has been devoted to the fabrication of full-cell LIBs using molecular self-assembly. Hammond et al. have LbL assembled polyaniline nanofiber/carbon nanotube (CNT) films as electrodes for LIB applications.^[22] They also showed a free-standing LbL assembled polyethylene oxide/polyacrylic acid multilayer film for LIB separators with Li⁺ conductivity up to 2.3×10^{-5} S cm⁻¹ at 52% relative humidity.^[23–24] Mo et al. reported a sandwich nanoarchitecture that was LbL self-assembled with LiV₃O₈ nanoparticles and graphene nanosheets on Ni foam for LIB cathode with a high reversible specific capacity (235 mAh g⁻¹ at 0.3 A g⁻¹).^[25] Liu et al. showed that stretchable Si-based anodes of LIBs could be formed by an LbL self-assembly of Si nanoparticles, Cu nanowires, and polyurethane into free-standing films.^[26] Using LbL self-assembly, they were able to avoid particle agglomeration and obtained a high specific capacity of 574 mAh g⁻¹ after 300 cycles at 1C from the anode. To further optimize electrode performances of LbL self-assembled LIBs, Cho group purposed the use of small molecules rather than the conventional high-molecular-weight polyelectrolytes to facilitate electron transport by minimizing the spacing between the electron conducting phase and the Li⁺ intercalating phase.^[27] However, the small molecule has been only demonstrated to

assemble particles smaller than 10 nm^[27–28] which is significantly smaller than the particle size of traditional battery materials (ranging from hundreds of nanometers to micrometers). Such small particle size is known to result in charge storage in a pseudocapacitive manner rather than the intercalative manner for traditional battery materials.^[29–30] No study has so far, presented a set of materials which are scalable and applicable to both LIB anode and cathode with typical Li⁺ intercalative characteristics, and which allow controlled positioning of the different phases, as well as allowing arbitrary substrates.

Here we study the fundamentals of the water-based LbL assembled electrodes on a planar substrate. The ability to self-assemble Li⁺ intercalating nanoparticles allows for a control over the composition of the electrodes at the nanoscale which results in a comparable electrode performance to the conventional slurry-cast electrode. We further show that the process of aqueous self-assembly can be used to fabricate the anode and cathode for a full-cell LIB inside 3D porous insulating substrates including foams and aerogels, which is not possible with slurry-casting. Finally, by systematically changing the distance between the conducting and intercalating phase using cations of different sizes, this work also demonstrates the potential for programmed self-assembly of nanoarchitectures for energy storage.

To build LIBs using LbL assembly, we need a complete set of active nanomaterials that can be dispersed and optimized in their colloidal properties for LbL self-assembly. In this study, we chose three Li⁺ intercalating materials: nanoparticles of lithium titanate (LTO, Li₄O₁₂Ti₅), lithium manganese oxide (LMO, LiMn₂O₄), and LFP (LiFePO₄), which are among the most popular Li⁺ intercalating materials for LIBs. We dispersed these nanoparticles in carboxymethyl cellulose (CMC) solutions. CMC acts mainly as a dispersing agent in the dispersions since its carboxymethyl (–OCH₂COO⁻) group forms complexes with the nanoparticles and adds negative charges to improve their dispersive stability.^[31] Besides its role as a dispersing agent, CMC also acts as a binder. As shown in Figure S1 and Table S1, Supporting Information, comparing with water-dispersed particles, CMC decreased the zeta-potential of the colloids to as low as –50 mV with enhanced colloidal stability, increased the weight concentrations of solids for a more efficient LbL assembly, and reduced the polydispersity indices (Table S1, Supporting Information) of the particles for an enhanced control over the nanostructure of the composite electrode. We note that even LFP, which is naturally less hydrophilic,^[32] can be dispersed and therefore the stability of the dispersion was enhanced by complexing LFP with CMC. CNTs were chosen as the electron conducting material, and were dispersed using CMC which is an excellent dispersing agent also for CNTs. The improved dispersive properties show that CMC is an excellent candidate for the dual purpose of acting as a binder as well as a dispersing agent for numerous nanoparticles in batteries.

We first prepared an LTO anode on a planar Ni foil by dip-coating (Figure 1a,b) which is assigned as (PEI1000k/LTO:CNT:CMC)₁₆₀ corresponding to 160 bilayers of two phases where the anionic phase was a mixed dispersion of LTO nanoparticles, CNTs, and CMC, and the cationic polyelectrolyte phase was branched-polyethyleneimine (PEI) of 600–1000 kDa, assigned as PEI1000k. This nanocomposite electrode had a thickness of 578 ± 58 nm (Figure 1c and Figure S3a, Supporting

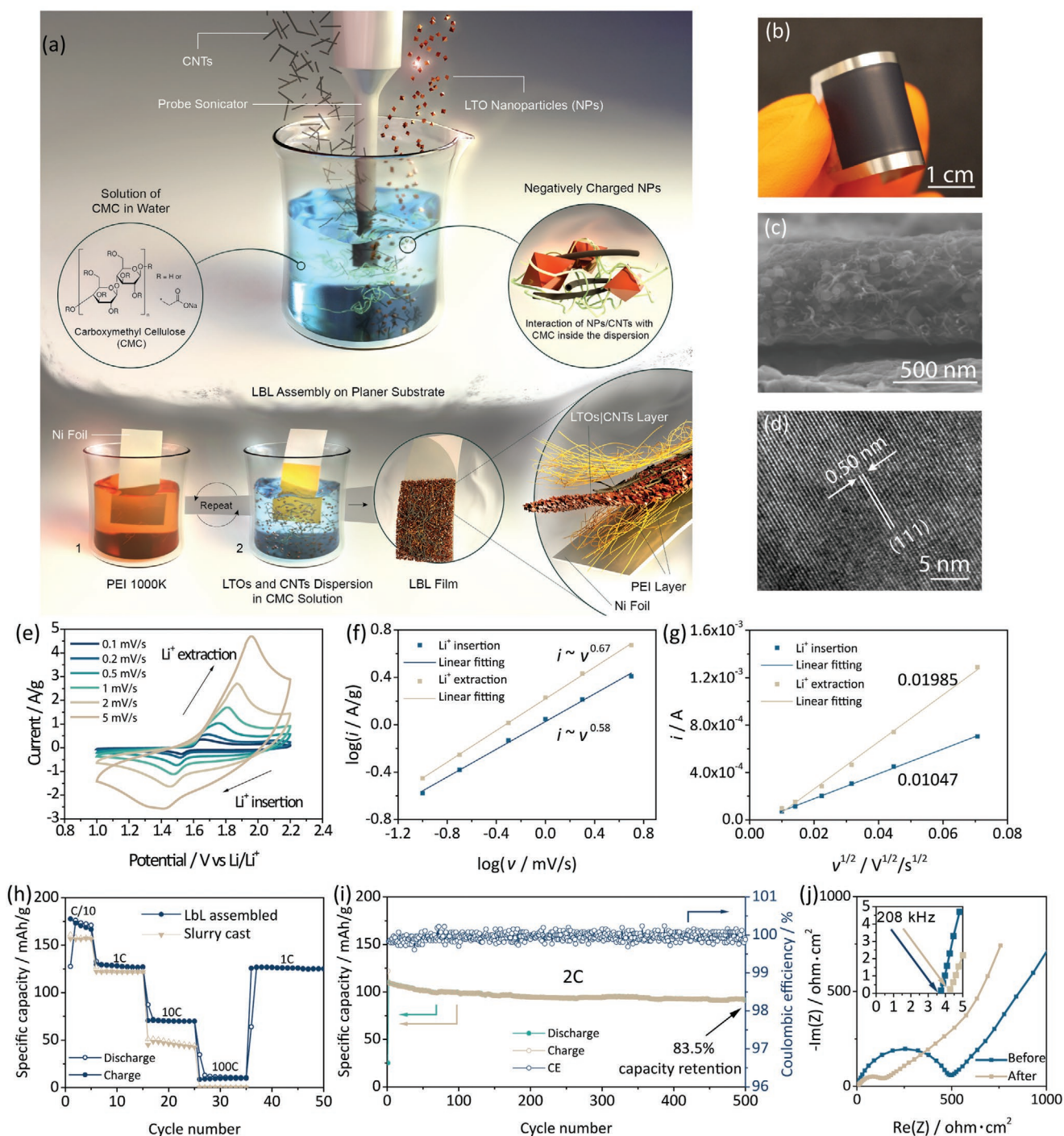


Figure 1. The LbL self-assembled LTO anode (PEI1000k/LTO:CNT:CMC)₁₆₀ on Ni foil: a) schematic illustration of LbL assembly process, b) photo, c) cross-sectional SEM image, d) HRTEM image, e) CV at various scan rates, f) peak current i as the function of the scan rate v from CV, g) peak current i as the function of the square root of scan rate $v^{1/2}$ from CV with the slopes shown in the chart, h) rate performance, i) 500 cycles of charge/discharge at 2C, and j) Nyquist plots before and after the 500 cycles of charge/discharge at 2C.

Information) and a mass loading of $0.17 \pm 0.02 \text{ mg cm}^{-2}$. The embedded LTO nanoparticles corresponded to 90 wt%, as determined by thermal gravity analysis (TGA, Figure S2, Supporting Information). Scanning electron microscopy (SEM) images (Figure S3b,c, Supporting Information) and transmission electron microscopy (TEM) images (Figure S3d, Supporting Information) of the electrodes showed a close contact between the

evenly distributed fine LTO nanoparticles and the CNTs. High-resolution (HR-) TEM images revealed a lattice fringe spacing of 0.50 nm which corresponds to the (111) plane of spinel LTO (Figure 1d). The selected-area electron diffraction (SAED) pattern (Figure S3e, Supporting Information) and X-ray diffraction (XRD) pattern (Figure S4, Supporting Information) shows typical crystalline peaks from LTO.

We packaged the electrode into a half-cell to characterize its electrochemical properties. Figure 1e shows the cyclic voltammetry (CV) of the (PEI1000k/LTO:CNT:CMC)₁₆₀ anode on Ni foil. The voltage window was between 1 and 2.2 V versus Li/Li⁺. In this window, only the conversion between Li₄Ti₅O₁₂ and Li₇Ti₅O₁₂ occurs and the contribution from the CNTs can be ignored (Figure S5, Supporting Information). The separation of peak potentials between Li⁺ insertion and Li⁺ extraction became wider when the scan rate increased from 0.1 to 5 mV s⁻¹. The peak current of Li⁺ extraction is higher than that of Li⁺ insertion, indicating slightly different kinetics between the lithiation and delithiation process. We analyzed the kinetics of the charge storage by considering a power-law relationship between the peak current and the scan rate ($i = av^b$),^[30] and obtained a “*b*-value” of 0.58 ($i \approx v^{0.58}$) for the Li⁺ insertion process (cathodic process, corresponding to discharge) and 0.67 ($i \approx v^{0.67}$) for the Li⁺ extraction process (anodic process, corresponding to charge) as shown in Figure 1f. The values correspond to a typical response for battery materials with diffusion-controlled kinetics (intercalation or solid-state diffusion followed by phase transition where the migration of Li⁺ inside the crystal lattices is the rate-determining step^[33]). Further, we correlated the peak currents (*i*) with the square root of scanning rate ($v^{1/2}$) and obtained a linear relation as shown in Figure 1g. The chemical diffusivity of Li⁺ for the insertion and extraction process was calculated to be 6.3×10^{-12} and 2.3×10^{-11} cm² s⁻¹, respectively, according to the Randles–Sevcik equation (see details in the Experimental Section).^[33] The diffusivity difference showed the Li⁺ extraction is faster than the insertion process, consistent with previous studies.^[34–35] During the Li⁺ insertion step, the phase-boundary moved from the Li₇Ti₅O₁₂ rock-salt shell towards the Li₄Ti₅O₁₂ spinel core and was controlled by the Li₇Ti₅O₁₂ phase which had a slower diffusivity. While in the Li⁺ extraction step, the boundary movement was controlled by the Li₄Ti₅O₁₂ spinel shell which delivered a faster diffusivity. In general, both the Li⁺ diffusivity values are comparable with and amongst the highest values for LTO anode.^[34,36–37] We attribute these high values to the readily available Li⁺ hosted by the amine groups of PEI1000k which are incorporated around the nanoparticles,^[38] as a consequence of the LbL self-assembly process using PEI1000k as the cationic compound.

This thin film anode showed a comparable performance to that from the conventionally slurry-casted LTO anode with the same LTO mass loading (see Experimental Section for details), delivering even slightly higher specific capacity during the charge/discharge cycles at all current densities ranging from C/10 to 100C (Figure 1h). The specific charging capacity at C/10 was 167 mAh g⁻¹ which is very close to the theoretical specific capacity of LTO (175 mAh g⁻¹), suggesting a nearly full intercalation of Li⁺ in the LTO nanoparticles. The LbL assembled LTO anode exhibit stable and controllable charge/discharge behavior even at 100C with a specific capacity of 11 mAh g⁻¹. At such a high rate, the characteristic potential plateau (Figure S6a, Supporting Information) was maintained during the delithiation process, indicating the charge storage induced a typical phase change of battery systems.^[39] At the same current density of 100C, the slurry-cast LTO anode (≈ 0.16 mg cm⁻² of LTO) could not maintain a stable potential, in the set range of 1–2.2 V in the charge/discharge profiles (Figure S6b, Supporting Information). The profiles showed typical capacitive behavior with a

low specific capacity of 0.5 mAh g⁻¹ and with no characteristic plateaus from battery electrodes. The current density of 100C was obviously too high for the slurry-cast electrode to intercalate Li⁺ into the LTO nanoparticles to maintain its battery-like charge/discharge manner. Instead, at such a high current density, the majority of the Li⁺ in the electrolyte shuttled between the Ni current collector and the counter electrode of Li foil, short-circuiting the layer of the electrode materials. Therefore, little charge could be stored in the capacitor formed by the two metal foils, making the charge/discharge time periods too short for the instrument to switch charge/discharge in time. In contrast, our LbL assembled anode could maintain the battery-like charge/discharge behavior due to the spontaneous arrangement of the ion intercalating phase and electron conducting phase by the self-assembly. We attribute the high performance of the LbL assembled anode to a combined result of: 1) having a thin electrode film where the ultrafine LTO nanoparticles and the electron conductor are all positioned with a nanometer precision; 2) having a PEI phase assembled in proximity to LTO nanoparticles, in which the lone pair of electrons in the N atoms could host Li⁺ as shown in Figure S7, Supporting Information, providing readily accessible Li⁺ for intercalation.^[38] The LbL assembled LTO anode retained 83.5% of the capacity of the 2nd cycle after 500 cycles at a charging/discharging rate of 2C (Figure 1i), prior to which the electrode was activated by 5 cycles of charge/discharge at C/10. The moderate capacity retention has been commonly observed in nanometer-sized and uncoated LTO batteries.^[40–43] The coulombic efficiency (CE) of the anode was higher than 99.6% from the 2nd to the 500th cycle, indicating highly reversible battery reactions. The Nyquist plot (Figure 1j) shows very low intrinsic resistance at the high-frequency range of 3.7 Ω·cm² which slightly increased to 4.2 Ω·cm² after the 500 cycles of charge/discharge, suggesting good conductivity and stability of the LbL assembled electrode. The charge transfer resistance on the other hand decreased drastically, which is the result of improved wetting of the electrolyte on the surface of the active material during the cycling.^[44–45] We note that the structure of LbL self-assembled electrodes is stable, because: 1) the polymers and nanoparticles have a high surface to volume area, and 2) because LbL operates based on multivalent electrostatic forces, so every layer including the first PEI layer, has a strong adhesion force to the next layer.

The study of planar LbL thin film electrodes with controlled architecture, and its comparison to the slurry-casted electrodes constitutes a rational route in the continued development and systematic study of self-assembly of nanocomposite battery electrodes. Compared to slurry casting, the LbL approach in this study has low efficiency for fabricating thicker electrodes. Our approach here is however limited by the output of the dipping robots for laboratory use, but this limitation can be overcome by employing spray coating or other industrial techniques in the future to achieve faster assembly of thicker electrodes.^[9]

We have previously shown that LbL self-assembly can be used to deposit various polymer solutions and dispersions of electronic materials inside the open-cell wall of an aerogel substrate.^[8] Comparing with the widely used in situ assemble nanostructures in metal foams,^[46–48] LbL assembly in polymer aerogels showed its advantages in light weight and independency of substrates. Using this technique we could control the

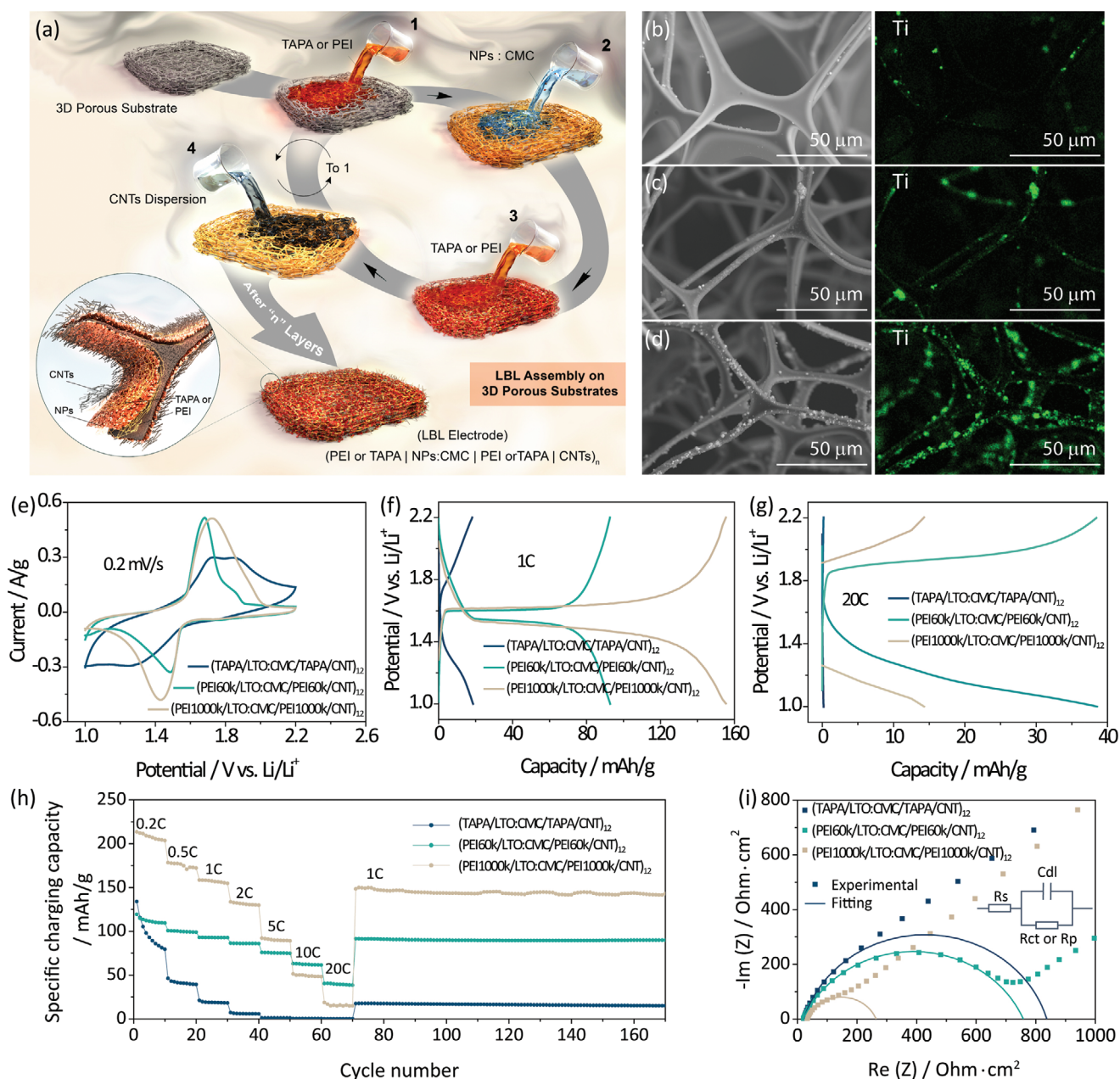


Figure 2. a) Schematics showing the LbL assembly on 3D porous substrates where NPs represents nanoparticles of LTO or LFP; SEM images (left column) and EDX element mapping of Ti (right column) showing the structure of the b) (TAPA/LTO:CMC/TAPA/CNT)₁₂ anode, c) (PEI60k/LTO:CMC/PEI60k/CNT)₁₂ anode, and d) (PEI1000k/LTO:CMC/PEI1000k/CNT)₁₂ anode; e) CV, f) charge/discharge profiles at 1C, g) charge/discharge profiles at 20C, h) rate performances, and i) Nyquist plots of the LTO anodes assembled with different cationic compounds (inset: the equivalent circuit for the fitting).

growth of the electrodes and the separator on the interior surface of an aerogel to form a full 3D supercapacitor.^[18] In this work, we demonstrate the versatility of LbL assembly to fabricate uniform LIB electrodes into non-conductive 3D porous substrates (Figure 2a). The formation of uniform thin films with nanometer precision inside 3D architecture is simply not possible with slurry casting. We chose melamine resin foam (MRF), with an average pore size of $230 \pm 86 \mu\text{m}$ and a porosity of 99.4%, as a model substrate because it is mechanically resilient and has a large pore size which enables easy and fast flow through its open pores and is thus suitable for the rapid

vacuum filtration-assisted LbL assembly method^[8] that we used to fabricate the electrodes inside the foam.

In this LbL process, we used cationic counterparts to reverse the charge between each layer containing the active particles. The cationic compounds were crucial, as their molecular sizes determined the resolution of the tailored nanostructure of the electrode.

We, therefore, investigated the properties of LTO anodes LbL assembled with three cations of different molecular mass: i) tris(3-aminopropyl)amine (TAPA), 188 g mol^{-1} , ii) PEI60k, and iii) PEI1000k. The assembled anodes are assigned (TAPA/LTO:CMC/TAPA/CNT)₁₂, (PEI60k/LTO:CMC/PEI60k/CNT)₁₂,

and (PEI1000k/LTO:CMC/PEI1000k/CNT)₁₂, respectively. The hydrodynamic diameters of the amines, determined by the dynamic light scattering technique, were 0.7 ± 0.1 , 11.5 ± 3.6 ,^[49] and 15.2 ± 4.5 nm (Figure S8, Supporting Information) respectively. In the dry state, our previous study showed that TAPA increased the average interlayer spacing of the LbL self-assembled MXene thin films by around 1 Å while PEI60k increased the spacing by 8.71 Å,^[21] which made it possible to control the spacing between consecutive layers in the nanometer precision, as schematically illustrated in Figure S9, Supporting Information. The SEM images and the corresponding elemental mapping of Ti in Figure 2b–d show a higher-molecular-weight amine could assemble a larger number LTO on the surface of MRF. TAPA resulted in the most sparsely assembled LTO particles, compared to the PEI counterparts. Determined by TGA (Figure S10, Supporting Information), LTO nanoparticles had a fraction of 12.8 wt% (0.43 mg cm^{-2}) of the (PEI1000k/LTO:CMC/PEI1000k/CNT)₁₂ anode, whereas 9.7 wt% (0.27 mg cm^{-2}) of the (PEI60k/LTO:CMC/PEI60k/CNT)₁₂ anode and 4.1 wt% (0.20 mg cm^{-2}) of the (TAPA/LTO:CMC/TAPA/CNT)₁₂ anode. Though TAPA had higher charge density of 21 meq g^{-1} than 18 meq g^{-1} of PEI60k,^[49] apparently polyelectrolytes with higher molecular weights have more charges per molecule which promise more stable assembly.

We tested the electrochemical properties of the anodes in the half-cell configuration. As shown in Figure 2e, (PEI60k/LTO:CMC/PEI60k/CNT)₁₂ displayed a typical oxidation (Li^+ extraction) peak centered at 1.68 V versus Li/Li^+ which corresponded to the conversion from $\text{Li}_7\text{Ti}_5\text{O}_{12}$ to $\text{Li}_4\text{Ti}_5\text{O}_{12}$ with a peak current of 0.52 A g^{-1} . The reduction peak (Li^+ insertion, converting $\text{Li}_4\text{Ti}_5\text{O}_{12}$ to $\text{Li}_7\text{Ti}_5\text{O}_{12}$) centered at 1.48 V with a current of 0.33 A g^{-1} . (PEI1000k/LTO:CMC/PEI1000k/CNT)₁₂ showed a typical extraction peak at 1.72 V with a peak current of 0.51 A g^{-1} and an insertion peak at 1.43 V with a current of 0.48 A g^{-1} . PEI60k delivered a preferred narrower peak separation but also an undesired smaller peak area, compared to PEI1000k. Both the anodes assembled with PEI60k and PEI1000k showed more significant redox peaks than those detected from the (TAPA/LTO:CMC/TAPA/CNT)₁₂, which indicated that Li^+ insertion/extraction dominated the electrochemical reactions of the half-cell due to the sufficient mass loading of the relatively larger LTO nanoparticles. The (TAPA/LTO:CMC/TAPA/CNT)₁₂ anode exhibited pseudocapacitive characteristics in CV with less distinctive redox peaks because of the relatively smaller particle size of LTO.^[29–30]

As shown in Figure 2f–h, when charging (Li^+ extraction) at 1C, the (PEI1000k/LTO:CMC/PEI1000k/CNT)₁₂ anode and the (PEI60k/LTO:CMC/PEI60k/CNT)₁₂ anode delivered a specific capacity of 155 and 93 mAh g^{-1} , respectively, while at 20C, the anodes delivered 14 and 38 mAh g^{-1} , respectively. PEI1000k endowed the anode with a high specific capacity at a low rate where its large contact resistance did not lead to large capacity loss. At 20C, the large size of the insulating polymer, PEI1000k, hindered the efficient electron transport, leading to significant capacity loss. PEI60k, benefitting from the smaller molecular size, showed a better rate performance. In contrast, the (TAPA/LTO:CMC/TAPA/CNT)₁₂ anode with the minimum contact spacing showed poor capacity of 18 mAh g^{-1} at 1C and 0.2 mAh g^{-1} at 20C, which is a strong indicator of the importance

of sufficient active materials mass loading. The higher-molecular-weight polyelectrolytes also showed better cyclic stability. During the last 100 cycles of charge/discharge at 1C, (PEI1000k/LTO:CMC/PEI1000k/CNT)₁₂ retained 96% of its capacity, while (PEI60k/LTO:CMC/PEI60k/CNT)₁₂ 98% and (TAPA/LTO:CMC/TAPA/CNT)₁₂ 86%. As shown in Figure S13, Supporting Information, excluding the first cycle of each C-rate, the (TAPA/LTO:CMC/TAPA/CNT)₁₂ anode delivered the lowest columbic efficiency, indicating the battery performances were significantly affected by the parasitic reactions, for example, the decomposition of the electrolyte. The latter can be naturally caused by the mismatch of the Fermi level of Li and the lowest unoccupied molecular orbital of electrolytes.^[16,50] The (PEI60k/LTO:CMC/PEI60k/CNT)₁₂ anode had the highest CE (>99.3%) at all the current densities, suggesting a highly reversible charge/discharge behavior at different rates. The (PEI60k/LTO:CMC/PEI60k/CNT)₁₂ anode showed high CE at low current densities but became less reversible at high current densities as the resistive losses became more prominent.

Our previous studies showed that TAPA minimized the spacing between different layers of the LbL assembled CNT^[49] and MXene^[21] electrodes for supercapacitors. Compared to PEI60k, TAPA delivered a four-fold higher conductivity for the CNT thin film with one-third of the CNT content. The modeling revealed two orders of magnitude lower contact resistance among the assembled CNT bundles.^[49] Nevertheless, the improved electronic conductivity by TAPA did not necessarily correlate to enhanced battery performances as discussed above. With electrochemical impedance spectroscopy (EIS), we investigated the kinetics of the half-cells by comparing the charge transfer resistance—the parameter indicating the difficulty for electrons/ Li^+ to migrate between the LTO nanoparticles and the current collector/electrolyte. We fit the Nyquist plots of the LbL assembled anodes using a simplified Randles cell model as shown in Figure 2i. While the molecular weight of the amine decreased from PEI1000k to PEI60k to TAPA, the charge transfer resistance (R_{ct}) increased from 232 to 815 ohm cm^2 , as listed in **Table 1**, suggesting decreasing Li^+ intercalation due to the lack of accessible LTO for intercalation. The fitting clearly indicated the fundamental importance of sufficient active materials loading to battery performances.

For the cathode counterparts, we designed and assembled (TAPA/LFP:CMC/TAPA/CNT)₂₀, (PEI60k/LFP:CMC/PEI60k/CNT)₁₂, and (PEI1000k/LFP:CMC/PEI1000k/CNT)₈ on MRF with LFP mass loading of 1.6, 12.7, and 7.2 wt%, respectively. Though we assembled the highest 20 tetra-layers for the (TAPA/LFP:CMC/TAPA/CNT)₂₀ cathode, TAPA could only assemble the smallest amount of LFP nanoparticles. From the CV curves scanned at 0.2 mV s^{-1} shown in Figure S14, Supporting Information, we

Table 1. Fitting parameters of the components in the simplified Randles cell models.

Anode	R_s [ohm cm^2]	R_{ct} [ohm cm^2]	C_{dl} [μF]
(TAPA/LTO:CMC/TAPA/CNT) ₁₂	21.5	815	9.3
(PEI60k/LTO:CMC/PEI60k/CNT) ₁₂	19.6	739	20
(PEI1000k/LTO:CMC/PEI1000k/CNT) ₁₂	32.0	232	18
(PEI1000k/LTO:CMC/TAPA/CNT) ₁₂	4.3	204	29

observed the largest area and the broadest redox peaks from the (PEI1000k/LFP:CMC/PEI1000k/CNT)₈ cathode, corresponding to the transition of the Fe²⁺/Fe³⁺ couple during the Li⁺ insertion and extraction process. The (TAPA/LFP:CMC/TAPA/CNT)₂₀ cathode showed the narrowest redox peaks with the smallest separation of 0.14 V and the largest proportion of the pseudocapacitive contribution among the three cathodes. The redox responses from the LFP cathodes assembled with different amines were highly consistent with those from the LTO anodes. The peak separation are associated with the interactions created by different counter ions, and the energy barrier for ion transport as well as electronic conductivity as we have discussed in this work. The (PEI1000k/LFP:CMC/PEI1000k/CNT)₈ cathode had the largest peak area

which promises a high charge/discharge capacity at a low current density. On the other hand, its larger peak separation and the broader redox peaks also indicate a higher energy barrier for the Li⁺ to reach the intercalation/redox sites inside the active materials, which may limit the charge/discharge performance of the electrode at a high rate.

Based on the findings, we further optimized the self-assembly design and fabricated (PEI1000k/LTO:CMC/TAPA/CNT)₁₂, schematically shown in Figure 3a. In this design, we hypothesized that PEI1000k would assemble larger LTO particles and increasing loading, while TAPA would provide a more intimate contact between the LTO particles and CNTs resulting in better electronic properties and faster kinetics. The SEM image, Figure 3b, showed that the pore structure

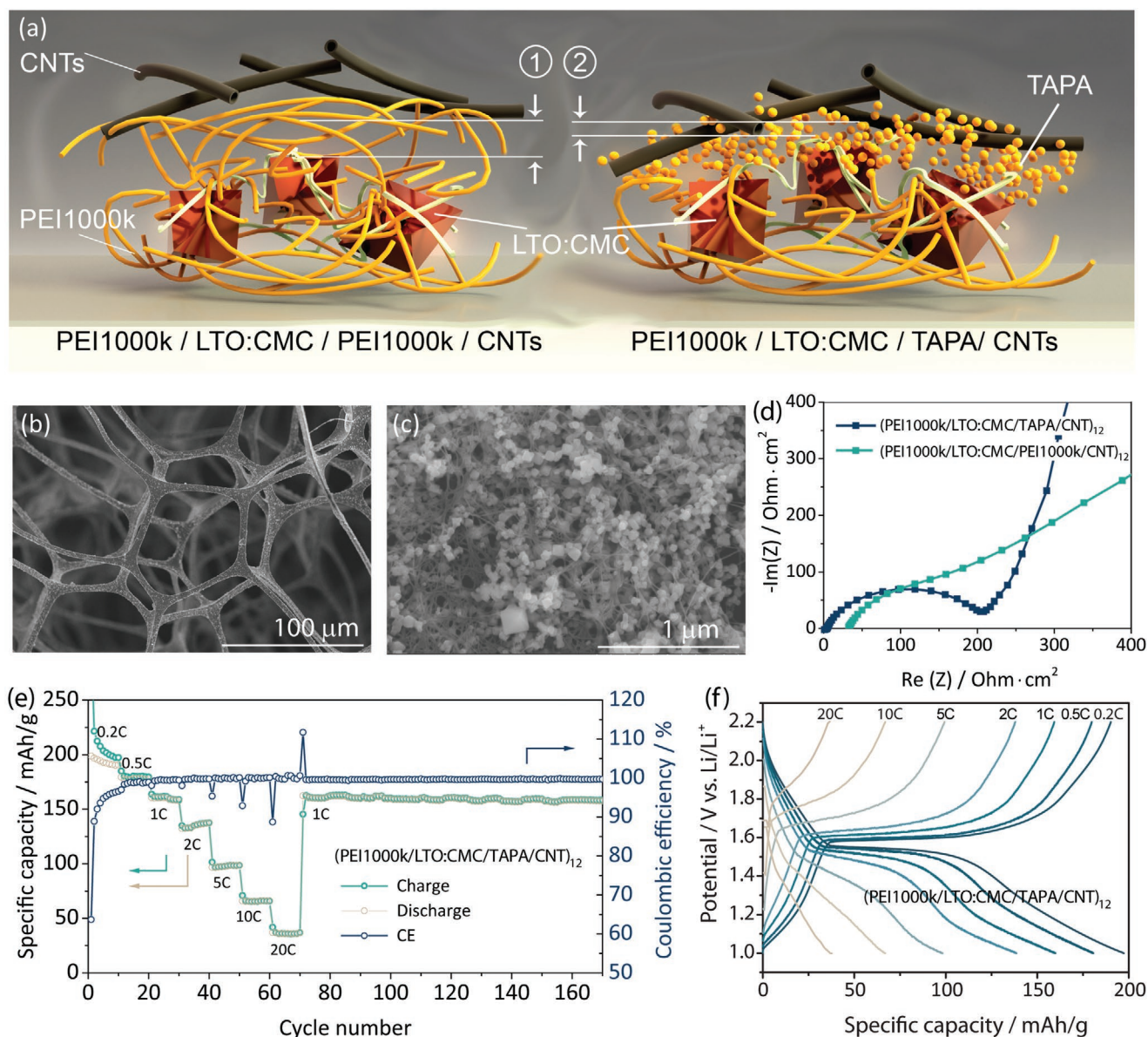


Figure 3. a) Schematic illustration of the structural differences between the LbL assembled anode (PEI1000k/LTO:CMC/PEI1000k/CNT)₁₂ and (PEI1000k/LTO:CMC/TAPA/CNT)₁₂; b, c) SEM images, d) Nyquist plot, e) the rate performance, and f) the charge/discharge profiles of the (PEI1000k/LTO:CMC/TAPA/CNT)₁₂ anode.

of the MRF was maintained after the LbL assembly while Figure 3c showed that abundant LTO nanoparticles ($11.1 \text{ wt}\%$, $0.37 \text{ mg LTO cm}^{-2}$) were in close contact with CNTs and had good coverage on the skeleton of the MRF. The Nyquist plot (Figure 3d) showed much lower electrolyte resistance (R_s) of 4.3 ohm cm^2 from the (PEI1000k/LTO:CMC/TAPA/CNT)₁₂ anode than the counterparts that were LbL assembled with one single amine (Table 1), indicating the programmed assembly decreased the comprehensive resistance of the half-cell significantly. We also observed lower charge transfer resistance of 204 ohm cm^2 due to the improved contact between the CNTs and the readily accessible LTO nanoparticles. Moreover, when charging/discharging (PEI1000k/LTO:CMC/TAPA/CNT)₁₂ at 1C (Figure 3e,f), the over potential of the anode was as low as 0.07 V and the specific capacity was as high as 159 mAh g^{-1} , which is 90% of the theoretical specific capacity of LTO. The anode delivered a specific capacity of 37 mAh g^{-1} at a high current density of 20C which is significantly higher than 15 mAh g^{-1} , the capacity of (PEI1000k/LTO:CMC/PEI1000k/CNT)₁₂, indicating an improved rate performance by introducing the small molecule TAPA to facilitate electron transport. At 10C, the insulating MRF-borne (PEI1000k/LTO:CMC/TAPA/CNT)₁₂ had a specific capacity of 66 mAh g^{-1} which is much higher than $\approx 45 \text{ mAh g}^{-1}$ of the slurry-cast LTO anode on the Ni foil (Figure 1h), owing to the optimized electrode structure. It should be noted that there was some capacity loss during the first few cycles, which could be the consequence of the reaction between Li^+ and the trace amount of $\text{H}_2\text{O}/\text{OH}$ species^[51] formed when transferring the electrodes into the glovebox because the electrode was composed of hygroscopic polymers and nanoparticles. Nevertheless, after the first few cycles, the anode exhibited good cyclic stability, retaining 97% of the capacity at 1C after 150 cycles in total of charge/discharge at various current densities (Figure 3e).

The two different electrodes (PEI1000k/LTO:CMC/TAPA/CNT)₁₂ and (PEI1000k/LTO:CMC/PEI1000k/CNT)₁₂ have identical active particles (LTO and CNT), and similar weight fraction between these particles, but the performance of (PEI1000k/LTO:CMC/TAPA/CNT)₁₂ is better because TAPA enables higher packing between the conducting phase and the intercalating phase. We note that, however, the improvement could only be realized on the basis of the abundant Li^+ intercalating nanoparticles that could be effectively assembled by the high-molecular-weight polyelectrolyte, PEI1000k. These results showed the advantage of LbL assembly over conventional approaches in precise assembling and positioning the different phases. This level of control is not possible with random mixing and slurry casting.

To demonstrate self-assembly as a technique towards full-cell batteries with good mechanical resilience, we sandwiched an LbL assembled anode (PEI1000k/LTO:CMC/PEI1000k/CNT)₁₂ and cathode (PEI1000k/LFP:CMC/PEI1000k/CNT)₁₂ in MRF with a commercial PE separator (Figure 4a). The apparent densities of the anode and cathode in MRF were 11.9 and 9.1 mg cm^{-3} , respectively. This LIB was compressible due to the 3D architecture and inherent properties of the porous substrates. We could therefore evaluate the battery performances under compression up to a deformation of 90%, as shown in Figure 4b–f. The full-cell battery delivered a discharge capacity of 45 mAh g^{-1} based on the total mass of LTO and LFP at 1C when uncompressed (Figure 4g and Figure S15, Supporting

Information). The discharge capacity decreased to 4 mAh g^{-1} at a higher current density of 10C and recovered to 43 mAh g^{-1} after applying 1C current density and retained 95.4% of the capacity after cycling at 1C for 50 cycles.

Under compression, the battery electrodes showed a robust structural stability (Figure 4g) and exhibited a considerable improvement in its rate performance, delivering a capacity of 36 mAh g^{-1} at 10C. At a low current density of 1C, we also observed an increase in the capacity to 56 mAh g^{-1} , compared to 45 mAh g^{-1} for the uncompressed battery. It has been proposed that compact electrodes are favored for improving battery performances because it facilitates the electron transport between the conductor and the active materials.^[4]

In addition to compression, we tested the resilience of the pouch battery by hitting the electrode area with a free-falling metal ball weighing 628 g from a height of 50 cm . This impact delivered an energy of 3.1 J and applied an estimated average force of 603 N to the electrode. After the impact, the (PEI1000k/LTO:CMC/TAPA/CNT)₁₂ anode remained fully functioning and showed no capacity loss when it was charged/discharged at 1C, as shown in Figure 4i and Figure S16, Supporting Information. The battery also maintained its functionality which is indicated by the connected light-emitting diode (Figure 4j).

Here, we show that aqueous LbL self-assembly can be used to prepare both anodes and cathodes of LIBs. This LbL assembly method utilizes aqueous dispersions of anionic nanoparticles, LTO, LMO, and LFP as the Li^+ intercalating phase, and anionic CNTs as the electron conducting phase. These dispersed particles were assembled using charged amines of different molecular sizes as the cationic component in the nanostructured multilayers. This fabrication scheme has three advantages: 1) It uses only water as solvent towards a greener fabrication route for LIBs. 2) It allows for optimal and precise positioning of the electrode components, including ion intercalating phase and electron conducting phase, therefore, offering superior control for the optimization of electrode performances to those obtained from conventionally slurry-cast electrodes. We could for example design an electrode with 12 consecutive quad-layers of (PEI1000k/LTO:CMC/TAPA/CNT)₁₂ with the rationale that a small molecule TAPA was used to assemble the CNT layer to minimize the distance between electron conductors and the Li^+ intercalating particles to sub-nanometer for a higher power density,^[49] and a large polyelectrolyte PEI1000k was used to encapsulate the large LTO lithium intercalating phase for a higher energy density. 3) It allows the controlled formation of multilayers onto arbitrary surfaces: we showed that complex 3D porous substrates such as foams and aerogels could be used as substrates allowing 3D electrodes with promising features, such as compressibility and resilience to impact.

To summarize, this work shows that aqueous self-assembly is a viable route for the next generation of batteries where programmed positioning of the phases in the electrode on any surface becomes possible. Many other dispersed nanoparticles beyond those used here can be explored such as 1D^[52] to 2D^[53–54] materials. The approach of LbL self-assembly can also be extended to other battery systems, including sodium-ion batteries,^[55] aluminum-ion batteries,^[56] zinc-ion batteries.^[57] Finally, aqueous self-assembly is a path towards realizing full 3D nanostructured batteries.^[4,18,39]

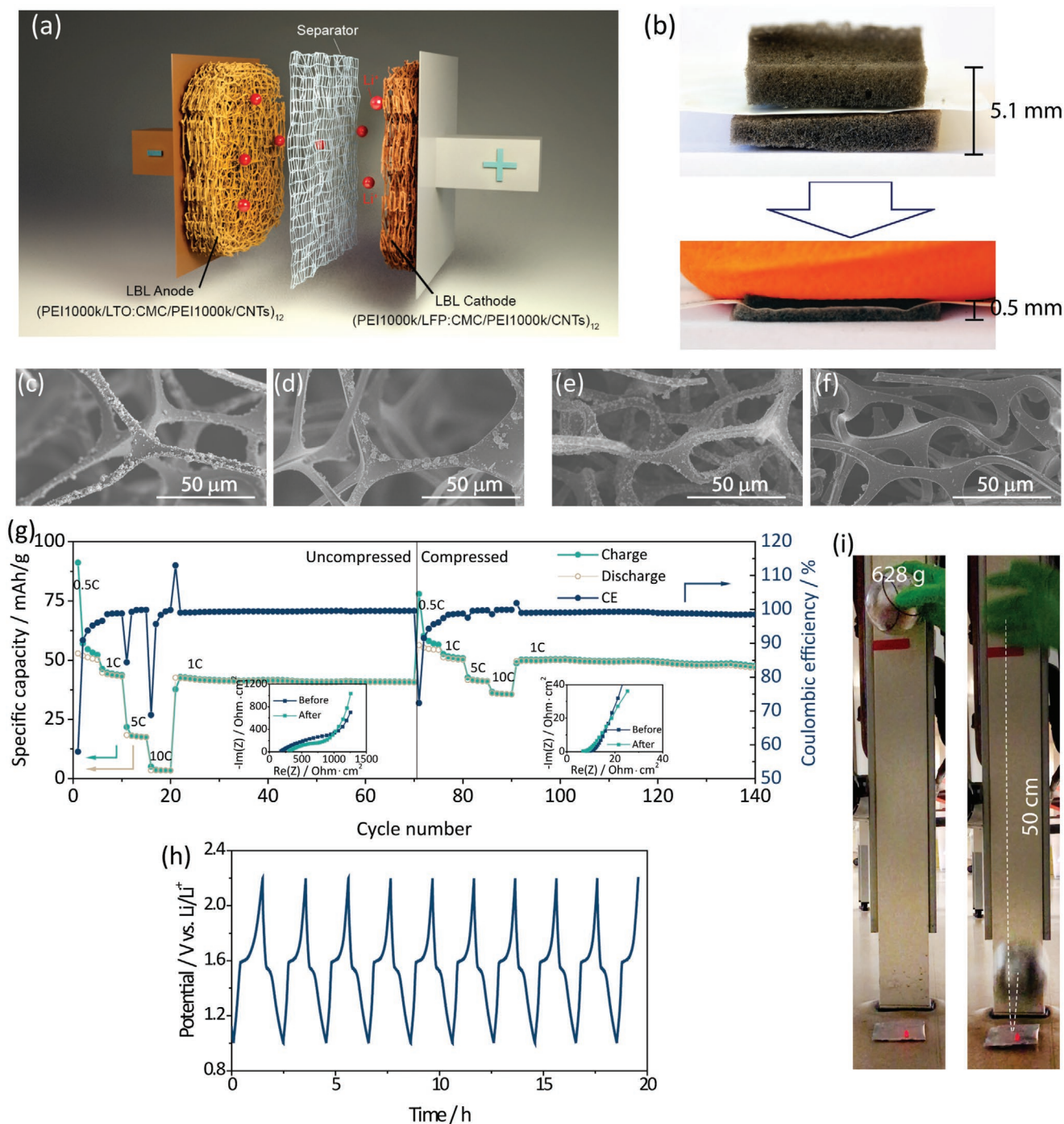


Figure 4. a) Schematics showing the battery structure; b) photos of the uncompressed and compressed LBL assembled LTO anode and LFP cathode with a separator in between; SEM images of the uncompressed c) LTO anode and d) LFP cathode and the compressed e) LTO anode and f) LFP cathode; g) cyclic stability at different rates of the uncompressed and compressed full cell. Inserts show the impedance change before and after the cycling; h) 10 cycles of charge/discharge profiles of the Lbl assembled LTO anode (PEI1000k/LTO:CMC/TAPA/CNT)₁₂ after smashing the electrode area with the free-falling metal ball from 50 cm height; and i) photos showing a full cell remains lighting an LED after being hit by the free-falling ball.

Experimental Section

Materials: LTO (>99%), LFP (>97%), CMC (sodium salt, typical Mw 90 000), and multi-wall CNTs with >8% carboxylic acid functionalized were purchased from Sigma-Aldrich. Tris(3-aminopropyl)amine (TAPA)

was a product from ChemCruz. Branched polyethyleneimine (PEI) of 60 kDa and 600–1000 kDa were from Acros Organics and Alfa-Aesar, respectively. Recticel AB, Sweden, generously provided the MRF (Basotect, BASF). CNF, in a gel state with 2 wt% of nanocellulose in water, was prepared by Innventia AB, Sweden using a high-pressure

homogenization technique.^[58] Charged carboxylic groups (600 $\mu\text{eq g}^{-1}$) was introduced to the CNF by treating the sulfite-dissolving pulp of softwood with mono-chloroacetic acid. Ultrapure water was used in this work.

Characterizations: A Hitachi S-4800 field-emission scanning electron microscope (SEM) was used to study the micromorphology. The element analysis from the energy-dispersive X-ray spectroscopy was obtained using X-MaxN range of silicon drift detectors from Oxford instruments at an accelerating voltage of 15 kV. The TEM study of the composites of CNTs and $\text{Li}_4\text{Ti}_5\text{O}_{12}$ was carried out using a 200 kV JEOL JEM-2100F microscope with an HR pole-piece ($C_s = 0.5$ mm) and a Schottky field-emission gun. Gatan Ultrascan 1000 CCD and Orius 100D camera were used to take TEM images and SAEDs, respectively. The composites were scratched off using a diamond scribe and then deposited onto a TEM grid with holey carbon supporting films. Particle size distributions and Zeta-potential were determined with a Malvern Zetasizer Nano ZS. The XRD patterns were collected with a PANalytical X'Pert PRO powder diffractometer with a $\text{Cu-K}\alpha$ source (wavelength 1.54178 Å). It was determined that the mass of active materials loaded into the substrates with TGA run in air on a Mettler Toledo TGA/DSC 1 at a ramping temperature of $10^\circ\text{C min}^{-1}$.

Preparation of the Solutions: Solutions of Amines: TAPA, PEI60k, and PEI1000k were dissolved into water with a concentration of 1 g L^{-1} and use hydrochloric acid (0.5 M HCl) to adjusted pH to 7.5.

Dispersion of CNTs: The carboxylic-functionalized CNTs were dispersed in water with an initial concentration of 2 g L^{-1} . Ultra Turrax T25 (IKA) was used to stir the suspension at 25 000 rpm for 10 min, following with ultra-sonication (Sonics, model CV33) for 20 min at 50% amplitude with an ice bath. The supernatant was collected after centrifuging the suspensions at 20 000 rpm for 1 h. Then supernatant was diluted to 0.2 g L^{-1} and used it as the dispersion of CNTs.

Mixture Dispersion of LTO, CNTs, and CMC: LTO and CNTs were dispersed in CMC solution with the initial solid content of 1 g L^{-1} of LTO, 0.5 g L^{-1} of CNTs, and 0.2 g L^{-1} of CMC. The suspensions were stirred with Ultra Turrax T25 at 25 000 rpm for 10 min, following with ultra-sonication (Sonics, model CV33) for 20 min at 50% amplitude in an ice bath. The supernatant was collected after centrifuging the suspension at 1500 rpm for 15 min.

Dispersions of the Li^+ Intercalating Nanoparticles: The electrochemically active nanoparticles were dispersed in CMC solution where CMC helps to improve the stability of the dispersions. Powder of LTO and LFP were added into CMC solutions (0.2 g L^{-1}) with initial concentration of 1 g L^{-1} , respectively. Then the suspensions were stirred with Ultra Turrax T25 at 25 000 rpm for 10 min, following ultra-sonication (Sonics, model CV33) for 20 min at 50% amplitude in an ice bath. The particle size and zeta-potential were determined with a Malvern Zetasizer Nano ZS.

Fabrication of Planar Electrodes: LbL assembly was carried onto Ni foil with the assistance of a dipping robot, StratoSequence VI. Before the assembly, the Ni foil was cleaned by ultra-sonicating in acetone for 10 min. The Ni foil was immersed into the solution PEI1000k of 1 g L^{-1} for 3 min, followed by rinsing three times with pure water for 2 min each. Then the foil was immersed into the mixture dispersion of LTO, CNT, and CMC for 3 min, followed by the same rinsing procedure. The process was repeated to have 160 pairs of layers, namely 160 bilayers. To get uniform adsorption onto the surfaces, the Ni foils were spun while immersed.

LTO anode was slurry-cast on Ni foil as the control electrode of which the data was presented in Figure 1h. The slurry was an aqueous-based mixture of 80 wt% of LTO, 10 wt% of CNTs, and 10 wt% of CMC. The total mass loading was $\approx 0.2\text{ mg cm}^{-2}$.

Fabrication of CNF Aerogels: BTCA and SHP were mixed in the nanocellulose gel at a 1:1 mass ratio (BTCA) and 2:1 mass ratio (SHP), followed by 15 min of stirring using an Ultra Turrax T25 (IKA, Germany), at 10 000 rpm. The gel was subsequently frozen in aluminum forms using liquid nitrogen and then freeze-dried. Finally, the freeze-dried aerogel was heated to 170°C for 5 min, to permanently cure the ester cross-links. All aerogels were thoroughly rinsed with Milli-Q water after

the cross-linking, to ensure that the residuals from the cross-linking were washed out.

Fabrication of 3D Electrodes: LbL deposition was carried out in MRF and CNF aerogels using a previously described rapid filtration procedure^[8] to build the electrodes for the half-cell batteries and for the full-cell batteries, as schematically illustrated in Figure 3a. Here (TAPA/LTO:CMC/TAPA/CNT)₁₂ was taken as an example to describe the detailed procedure. 1) The cationic solution of TAPA, 2) the anionic dispersion of LTO:CMC, 3) the cationic solution of TAPA, and 4) the anionic dispersion of CNT were poured in sequence with a rinsing step between each two steps to build a quad-layers. The sequence was repeated until 12 quad-layers were gotten. The samples were flipped after every 2 quad-layers for a uniform deposition of the materials. The anodes were assigned as (TAPA/LTO:CMC/TAPA/CNT)₁₂. Anodes assigned as (PEI60k/LTO:CMC/PEI60k/CNT)₁₂ and (PEI1000k/LTO:CMC/PEI1000k/CNT)₁₂ were assembled in the same procedure using PEI60k and PEI1000k, respectively.

For LFP cathodes, it was assembled in the same procedure but with different numbers of quad-layers. The samples were assigned as (TAPA/LFP:CMC/TAPA/CNT)₂₀, (PEI60k/LFP:CMC/PEI60k/CNT)₁₂, and (PEI1000k/LFP:CMC/PEI1000k/CNT)₈.

Packaging of Batteries: All the batteries inside an argon-filled glovebox were packaged (MBraun Labstar) with both H_2O and O_2 levels lower than 1 ppm. The planar electrodes on Ni foil were assembled into coin cells (CR2032) while the 3D electrodes were assembled into pouch cells. All the electrode (anode or cathode) performances in the half-cell battery configuration were examined, which was constructed by the LbL assembled electrodes as the working electrodes and lithium foil (99.9%, Alfa-Aesar) as the counter electrode with a polyethylene separator between the electrodes. The full-cell battery was packed with the LbL assembled anode and cathode separated by a polyethylene separator. The batteries were soaked with 1 M LiPF_6 solution in EC/DEC (1:1) (Sigma-Aldrich), and were ready for performance tests after the pouches were sealed and left resting for 12 h.

Battery Performance Tests: Most of the battery tests were carried out on a Biologic VSP multichannel potentiostat equipped with EIS except the charge/discharge cycling of the (PEI1000k/LTO:CMC/TAPA/CNT)₁₂ anode which the measurement was conducted on a Land CT2001A battery testing system. 1C charge/discharge rate was defined as 148 mA g^{-1} for LMO, 175 mA g^{-1} for LTO, and 170 mA g^{-1} for LFP and calculated the specific capacity of the half-cells based on the mass of the active materials. For the full cells, 1C was defined as 175 mA g^{-1} and calculated the specific capacity based on the total mass of LTO and LFP. The capacity of the LFP cathode was excessive by 50% than the capacity of the LTO anode. The CE was determined by $C_{\text{delithiation}}/C_{\text{lithiation}}^*100\%$.

The EIS was carried out from 1 MHz to 10 mHz at the open-circuit voltages of the cells with an amplitude of 10 mV.

The Li^+ diffusivity was calculated from the Randles–Sevcik equation:

$$i = 0.4463n^{3/2}F^{3/2}CSR^{-1/2}\bar{D}_{CV}^{1/2}\nu^{1/2} \quad (1)$$

where i is the peak current (A), n is the charge transfer number, 3 in this case, F is the Faraday's constant ($96\,486\text{ C mol}^{-1}$), C is the concentration (0.001 mol cm^{-3}), S is the surface area of the electrode materials (2.835 cm^2), R is the gas constant ($8.314\text{ J (mol}\cdot\text{K)}^{-1}$), T is the temperature (297 K), \bar{D}_{CV} is the chemical diffusion coefficient ($\text{cm}^2\text{ s}^{-1}$) measured by CV, and ν is the scan rate (V s^{-1}).

It was evaluated that the cyclic stability of the LTO anode assembled on Ni foil by 5 cycles of charge/discharge at C/10 to activate the half-cell, following with 500 cycles of charge/discharge at 2C. EIS was run before and after the 500 cycles of charge/discharge to give the Nyquist plots.

Supporting Information

Supporting Information is available from the Wiley Online Library or from the author.

Acknowledgements

The authors acknowledge the European Research Council (Grant 715268), the Wenner-Gren Foundation, and Knut and Alice Wallenberg Foundation (through Wallenberg Wood Science Centre at KTH) for research funding and for an equipment grant for the electron microscopy facilities at Stockholm University. The authors thank Dr. Andrew Marais for taking some of the photos of the samples.

Conflict of Interest

The authors declare no conflict of interest.

Author Contributions

Z.W. designed and prepared the LbL assembled electrodes, conducted characterizations of the devices, analyzed the data, and wrote the manuscript under the supervision of M.H. A.V.M. made the schematic illustrations. L.O. organized the data. J.E. prepared the CNF aerogels. C.-W.T. designed and performed the TEM study. L.W. contributed to ideas and data interpretation particularly on the LbL system. All the authors contributed to the discussion of the results and to the writing of the manuscript.

Keywords

3D electrodes, compressible batteries, energy storage, nanomaterials, self-assembly

Received: October 15, 2020

Revised: November 24, 2020

Published online:

- [1] M. Armand, J. M. Tarascon, *Nature* **2008**, 451, 652.
 [2] J. M. Tarascon, M. Armand, *Nature* **2001**, 414, 359.
 [3] J. Liu, Q. Zheng, M. D. Goodman, H. Zhu, J. Kim, N. A. Krueger, H. Ning, X. Huang, J. Liu, M. Terrones, P. V. Braun, *Adv. Mater.* **2016**, 28, 7696.
 [4] J. W. Long, B. Dunn, D. R. Rolison, H. S. White, *Chem. Rev.* **2004**, 104, 4463.
 [5] C. Zhu, R. E. Usiskin, Y. Yu, J. Maier, *Science* **2017**, 358, eaao2808.
 [6] G. M. Whitesides, B. Grzybowski, *Science* **2002**, 295, 2418.
 [7] E. Pomerantseva, Y. Gogotsi, *Nat. Energy* **2017**, 2, 17089.
 [8] M. Hamed, E. Karabulut, A. Marais, A. Herland, G. Nyström, L. Wågberg, *Angew. Chem., Int. Ed.* **2013**, 52, 12038.
 [9] J. J. Richardson, M. Bjornmalm, F. Caruso, *Science* **2015**, 348, aaa2491.
 [10] F. X. Xiao, M. Pagliaro, Y. J. Xu, B. Liu, *Chem. Soc. Rev.* **2016**, 45, 3088.
 [11] G. Decher, *Science* **1997**, 277, 1232.
 [12] H. Lee, Y. Lee, A. R. Statz, J. Rho, T. G. Park, P. B. Messersmith, *Adv. Mater.* **2008**, 20, 1619.
 [13] W. Chen, S. Li, C. Chen, L. Yan, *Adv. Mater.* **2011**, 23, 5679.
 [14] S. Nardecchia, D. Carriazo, M. L. Ferrer, M. C. Gutierrez, F. del Monte, *Chem. Soc. Rev.* **2013**, 42, 794.
 [15] L. Liu, Z. Niu, J. Chen, *Chem. Soc. Rev.* **2016**, 45, 4340.
 [16] Z. Li, K. Jiang, F. Khan, A. Goswami, J. Liu, A. Passian, T. Thundat, *Sci. Adv.* **2019**, 5, eaav2820.
 [17] R. Wang, C. Xu, M. Du, J. Sun, L. Gao, P. Zhang, H. Yao, C. Lin, *Small* **2014**, 10, 2260.
 [18] G. Nyström, A. Marais, E. Karabulut, L. Wågberg, Y. Cui, M. M. Hamed, *Nat. Commun.* **2015**, 6, 7259.
 [19] Z. C. Qian, R. Li, J. Guo, Z. Wang, X. F. Li, C. C. Li, N. Zhao, J. Xu, *Nano Energy* **2019**, 64, 103900.
 [20] Z. Qian, M. Yang, R. Li, D. Li, J. Zhang, Y. Xiao, C. Li, R. Yang, N. Zhao, J. Xu, *J. Mater. Chem. A* **2018**, 6, 20769.
 [21] W. Tian, A. VahidMohammadi, Z. Wang, L. Ouyang, M. Beidaghi, M. M. Hamed, *Nat. Commun.* **2019**, 10, 2558.
 [22] M. N. Hyder, S. W. Lee, F. Ç. Cebeci, D. J. Schmidt, Y. Shao-Horn, P. T. Hammond, *ACS Nano* **2011**, 5, 8552.
 [23] J. L. Lutkenhaus, K. D. Hrabak, K. McEnnis, P. T. Hammond, *J. Am. Chem. Soc.* **2005**, 127, 17228.
 [24] D. M. DeLongchamp, P. T. Hammond, *Langmuir* **2004**, 20, 5403.
 [25] R. W. Mo, F. W. Zhang, Y. Du, Z. Y. Lei, D. Rooney, K. N. Sun, *J. Mater. Chem. A* **2015**, 3, 13717.
 [26] L. Liu, M. Li, L. Chu, B. Jiang, R. Lin, *Appl. Surf. Sci.* **2019**, 476, 501.
 [27] Y. Ko, M. Kwon, Y. Song, S. W. Lee, J. Cho, *Adv. Funct. Mater.* **2018**, 28, 1804926.
 [28] Y. Ko, M. Kwon, W. K. Bae, B. Lee, S. W. Lee, J. Cho, *Nat. Commun.* **2017**, 8, 536.
 [29] P. Simon, Y. Gogotsi, B. Dunn, *Science* **2014**, 343, 1210.
 [30] J. Wang, J. Polleux, J. Lim, B. Dunn, *J. Phys. Chem. C* **2007**, 111, 14925.
 [31] J. Li, R. B. Lewis, J. R. Dahn, *Electrochem. Solid-State Lett.* **2007**, 10, A17.
 [32] Y. Wang, Z. Y. He, Y. X. Wang, C. Fan, C. R. Liu, Q. L. Peng, J. J. Chen, Z. S. Feng, *J. Colloid Interface Sci.* **2018**, 512, 398.
 [33] K. Tang, X. Yu, J. Sun, H. Li, X. Huang, *Electrochim. Acta* **2011**, 56, 4869.
 [34] N. Takami, K. Hoshina, H. Inagaki, *J. Electrochem. Soc.* **2011**, 158, A725.
 [35] M. Z. Bazant, *Acc. Chem. Res.* **2013**, 46, 1144.
 [36] L. T. N. Huynh, C. T. D. Ha, V. D. Nguyen, D. Q. Nguyen, M. L. P. Le, V. M. Tran, *J. Chem.* **2019**, 2019, 1727859.
 [37] L. Youjie, R. Li, Y. Yang, Z. Li, *New J. Chem.* **2018**, 42, 15097.
 [38] W. Zeng, L. Wang, X. Peng, T. Liu, Y. Jiang, F. Qin, L. Hu, P. K. Chu, K. Huo, Y. Zhou, *Adv. Energy Mater.* **2018**, 8, 1702314.
 [39] M. R. Lukatskaya, B. Dunn, Y. Gogotsi, *Nat. Commun.* **2016**, 7, 12647.
 [40] L. Zhao, Y.-S. Hu, H. Li, Z. Wang, L. Chen, *Adv. Mater.* **2011**, 23, 1385.
 [41] Y. Wang, A. Zhou, X. Dai, L. Feng, J. Li, J. Li, *J. Power Sources* **2014**, 266, 114.
 [42] S. Cao, X. Feng, Y. Song, X. Xue, H. Liu, M. Miao, J. Fang, L. Shi, *ACS Appl. Mater. Interfaces* **2015**, 7, 10695.
 [43] L. Wang, Y. Zhang, H. Guo, J. Li, E. A. Stach, X. Tong, E. S. Takeuchi, K. J. Takeuchi, P. Liu, A. C. Marschillok, S. S. Wong, *Chem. Mater.* **2018**, 30, 671.
 [44] K. W. Knehr, T. Hodson, C. Bommier, G. Davies, A. Kim, D. A. Steingart, *Joule* **2018**, 2, 1146.
 [45] Z. Wang, A. Malti, L. Ouyang, D. Tu, W. Tian, L. Wågberg, M. M. Hamed, *Small* **2018**, 14, 1803313.
 [46] Z. Wu, L. Jiang, W. Tian, Y. Wang, Y. Jiang, Q. Gu, L. Hu, *Adv. Energy Mater.* **2019**, 9, 1900111.
 [47] P. Yang, Z. Wu, Y. Jiang, Z. Pan, W. Tian, L. Jiang, L. Hu, *Adv. Energy Mater.* **2018**, 8, 1801392.
 [48] Y. Liang, C.-Z. Zhao, H. Yuan, Y. Chen, W. Zhang, J.-Q. Huang, D. Yu, Y. Liu, M.-M. Titirici, Y.-L. Chueh, H. Yu, Q. Zhang, *InfoMat* **2019**, 1, 6.
 [49] Z. Wang, L. Ouyang, W. Tian, J. Erlandsson, A. Marais, K. Tybrandt, L. Wågberg, M. M. Hamed, *Langmuir* **2019**, 35, 10367.
 [50] J. B. Goodenough, *Acc. Chem. Res.* **2013**, 46, 1053.
 [51] W. J. H. Borghols, D. Lützenkirchen-Hecht, U. Haake, W. Chan, U. Lafont, E. M. Kelder, E. R. H. van Eck, A. P. M. Kentgens,

- F. M. Mulder, M. Wagemaker, *J. Electrochem. Soc.* **2010**, *157*, A582.
- [52] S. Srivastava, N. A. Kotov, *Acc. Chem. Res.* **2008**, *41*, 1831.
- [53] K.-S. Chen, I. Balla, N. S. Luu, M. C. Hersam, *ACS Energy Lett.* **2017**, *2*, 2026.
- [54] W. Tian, A. VahidMohammadi, M. S. Reid, Z. Wang, L. Ouyang, J. Erlandsson, T. Pettersson, L. Wagberg, M. Beidaghi, M. M. Hamed, *Adv. Mater.* **2019**, *31*, 1902977.
- [55] M. D. Slater, D. Kim, E. Lee, C. S. Johnson, *Adv. Funct. Mater.* **2013**, *23*, 947.
- [56] M. C. Lin, M. Gong, B. Lu, Y. Wu, D. Y. Wang, M. Guan, M. Angell, C. Chen, J. Yang, B. J. Hwang, H. Dai, *Nature* **2015**, *520*, 324.
- [57] D. Kundu, B. D. Adams, V. Duffort, S. H. Vajargah, L. F. Nazar, *Nat. Energy* **2016**, *1*, 16119.
- [58] L. Wågberg, G. Decher, M. Norgren, T. Lindström, M. Ankerfors, K. Axnäs, *Langmuir* **2008**, *24*, 784.